

Macro-meso dynamic analysis of railway transition zone: Hybrid DEM/FDM simulation and experimental validation

Shi, Can; Zhao, Chunfa; Yang, Yang; Guo, Yunlong; Zhang, Xu; Feng, Yang

DOI

[10.1016/j.soildyn.2020.106191](https://doi.org/10.1016/j.soildyn.2020.106191)

Publication date

2020

Document Version

Accepted author manuscript

Published in

Soil Dynamics and Earthquake Engineering

Citation (APA)

Shi, C., Zhao, C., Yang, Y., Guo, Y., Zhang, X., & Feng, Y. (2020). Macro-meso dynamic analysis of railway transition zone: Hybrid DEM/FDM simulation and experimental validation. *Soil Dynamics and Earthquake Engineering*, 135, Article 106191. <https://doi.org/10.1016/j.soildyn.2020.106191>

Important note

To cite this publication, please use the final published version (if applicable). Please check the document version above.

Copyright

Other than for strictly personal use, it is not permitted to download, forward or distribute the text or part of it, without the consent of the author(s) and/or copyright holder(s), unless the work is under an open content license such as Creative Commons.

Takedown policy

Please contact us and provide details if you believe this document breaches copyrights. We will remove access to the work immediately and investigate your claim.

Macro-meso dynamic analysis of railway transition zone: Hybrid DEM/FDM simulation and experimental validation

Can Shi¹, Chunfa Zhao^{1*}, Yang Yang², Yunlong Guo³, Xu Zhang⁴, Yang Feng¹

1. State Key Laboratory of Traction Power, Southwest Jiaotong University, Chengdu, Sichuan 610031, P.R. China

2. China Railway Eryuan Engineering Group CO. LTD, Chengdu, Sichuan 610031, P.R. China

3. Faculty of Civil Engineering and Geosciences, Delft University of Technology, Delft, 2628CN, Netherlands

4. School of Civil and Transportation Engineering, Guangdong University of Technology, Guangzhou, Guangdong 510006, P.R. China

* Corresponding author

E-mail addresses: shican@my.swjtu.edu.cn (C. Shi); cfzhao@home.swjtu.edu.cn (C.F. Zhao)

Abstract: To probe into the mechanical behaviour of railway transition zone from the macro-meso aspects, a numerical model of transition zone is built that hybrids the Discrete Element Method (DEM) and Finite Difference Method (FDM). The DEM is utilized to simulate the ballast bed and sleeper, because it can consider the realistic ballast shapes and complex contacts between them. The FDM based on the continuum theory is utilised to simulate the track substructure according to a real structural form. Afterwards, the coupling algorithm is used to achieve the hybrid DEM-FDM simulation. The engineering practicality of this model is validated using the dynamic responses of the transition zone from a field measurement, and the macro-meso mechanical behaviour of the transition zone is analysed with or without the wedge-shape backfill. The numerical results indicate that applying the wedge-shape backfill can considerably reduce the sudden changes of track vibration and substructure surface stresses at the vicinity of the connection between the structure and embankment. Moreover, the mesoscopic results show that the acceleration vector of the soil near the rigid structure fluctuates towards the embankment and the velocity responses of track components and substructure increase gradually when the train travels from the rigid structure to the soft embankment.

Keywords: Discrete element method; Finite difference method; Coupled modelling; Field measurement; Transition zone; Dynamic response

1. Introduction

In engineering practices, it was found that railway transition zones experience higher rate of track geometry degradation comparing to the normal track sections, and therefore require frequent inspections, maintenances and renewal. So far, numerous studies have been performed to solve the transition zone problem by providing gradual

1 stiffness change between the normal track and the stiffer structure. On the one hand, the less stiff sider is enhanced
2 to have a higher stiffness (e.g. applying backfills with higher deformation modulus). On the other hand, the track
3 rigidity of the stiffer sides is reduced (e.g. using under sleeper pads). However, transition zones still show
4 unsatisfying dynamic performances, and the problem of the transition differential settlements is far from being
5 solved.

6 Over the past decades, many scholars performed experimental and theoretical studies on transition zones to
7 investigate the processes of track degradation and dynamic behaviour. For the theoretical studies, some researchers
8 [1-3] applied the theory of dynamic coupling vehicle-track to analyse the dynamic behaviour of vehicle and the
9 interaction between the vehicle and the transition zone. In this case, the multi-layer track is considered as a series of
10 separated mass bulks linked with springs and dampers, by which the geometric and parametric characteristics of the
11 transition zone are simplified. Because of this, the track substructure cannot be appropriately simulated using the
12 vehicle-track coupling dynamic model. Alternatively, some other theoretical studies applied the finite element
13 method with the real substructure form [4-8]. This method is accurate for evaluating the global behaviour of the
14 transition zone, but cannot reveal the dynamic behaviour of the ballast bed from the mesoscopic level. For the
15 experimental studies, many experimental measurements at the transition zones [9-14] were performed to reveal the
16 dynamic characteristics and the settlement of the transition zone. These experimental studies presented some
17 valuable views on macromechanical dynamic behaviour and degradation mechanisms of railway ballast, but the
18 mesomechanical dynamic behaviour and its evolutionary process are almost impossible to observe from laboratory
19 measurements or field tests.

20 In summary, most of the earlier theoretical studies cannot sufficiently figure out the mesoscopic behaviour of
21 railway ballast at transition zones from the dynamic viewpoint, because they regarded the ballast bed as an elastic
22 continuum or layers of mass, springs and dampers. In other words, the discontinuity, inhomogeneity, and
23 randomness of granular ballast aggregates cannot be presented. Thus the ballast movements and contact force
24 redistribution under train loads are ignored. Regarding these limitations, the DEM is provided as a new approach
25 for studying the macromechanical and mesomechanical dynamic behaviour of ballast assemblies. It has been
26 widely utilised to study the mechanical behaviour of ballasted tracks [15]. For instance, some recent studies using
27 the DEM for the transition zone are presented in [16-17]. These studies provide an insight into internal factors that
28 affect the track transition settlement.

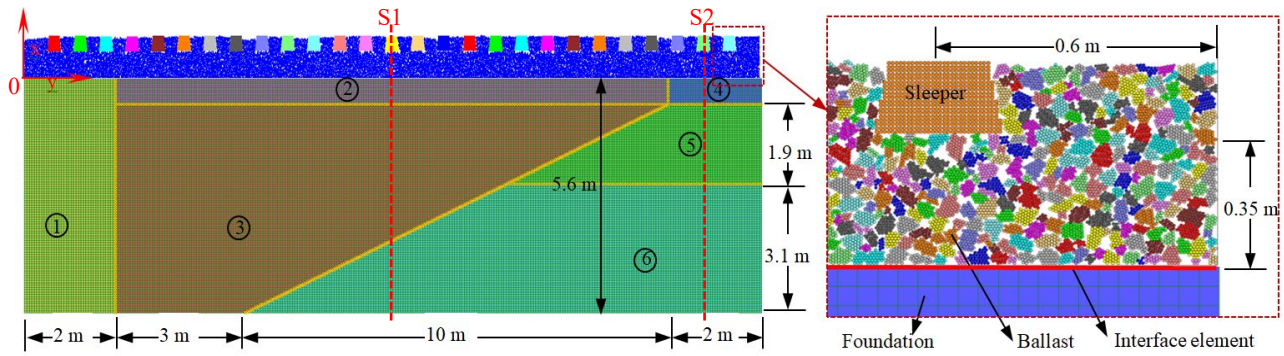
1 However, these DEM transition zone models did not consider the deformation of substructure, due to they
2 simplify the transition zone substructure as continuous supporting wall elements with different stiffness. The
3 substructure under the train load produces small elastic and plastic deformations, which can lead to the ballast
4 particles movements and the force chain redistribution. Because of this, the dynamic behaviour, settlement and
5 degradation rate of the transition zone are significantly affected. Therefore, the railway transition zone that can
6 consider the real substructure support condition is established in this paper. The DEM is used to simulate the ballast
7 bed and sleepers, and the FDM is applied to simulate the substructure of the transition zone as a continuous
8 medium. Then, the discrete-continuous coupled model is built by exchanging displacements, velocities and contact
9 forces between the DEM and the FDM. The reliability of this model is proved preliminarily by comparing with the
10 field test results, afterwards, the dynamic behaviour of the transition zone is analysed in two circumstances:
11 considering wedge-shape backfill or ignoring the wedge-shape backfill.

12 **2. Numerical modelling**

13 As depicted in Figure 1, the discrete-continuum coupled model of track transition is established by combining the
14 DEM with the FDM. The railway ballasted track (sleepers and ballast particles) is built with the software, Particle
15 Flow Code (PFC), and the substructure of the transition zone is built with the Fast Lagrangian Analysis of Continua
16 (FLAC). Considering the computational efficiency and the real dimension of the transition zone (according to the
17 Chinese railway design code [18]), the length of the track transition model is 17 m (27 sleepers) and the vertical
18 boundary walls (left and right sides) are 0.6 m away from the nearest sleeper. The longitudinal spacing between two
19 adjacent concrete sleepers is 0.6 m, and the thickness of the ballast bed is 0.35 m. The substructure consists of six
20 parts: the surface layer of the subgrade (0.6 m), the bottom layer of the subgrade (1.9 m), the subgrade body (3.1 m),
21 the surface layer of the subgrade for transition zone (0.6 m) the wedge-shaped backfill (5 m) and the structure (5.6
22 m). The structure (on the tunnel section) is simplified as a rectangle with the width of 2 m and its depth from the
23 ground is 5.6 m. The bottom length of wedge-shaped backfill is 3 m away from the structure, with a slope value at
24 1:2.

25

26



①. Structure ②. Surface layers of the subgrade for transition zone ③. Wedge-shaped backfill
 ④. Surface layers of the subgrade ⑤. Bottom layers of the subgrade ⑥. Subgrade body

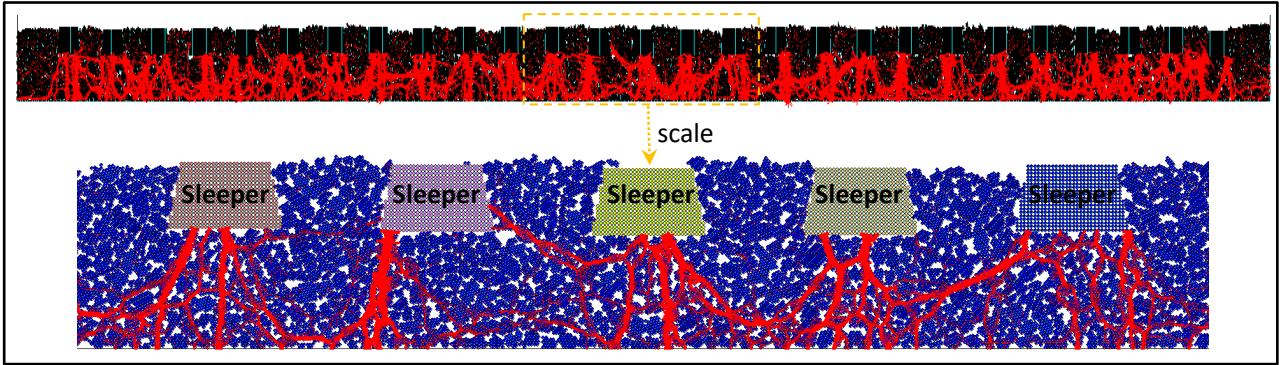
Fig. 1 The schematic longitudinal profile of the transition zone

2.1 Sleeper-ballast bed DEM model

The well-graded crushed stones selected for railway ballast always have irregular shapes, which have proven to be critical for the ballast bed strength and stability. To build a ballast particle with irregular shape, a technique of digital image analyses is used to simulate typical ballast shape [19]. The simulation technique of ballast with irregular shape can be found in reference [20]. The DEM part of railway ballasted track is simulated by the steps below: (1) a library of the DEM ballast samples is created using the image analysis technique in [20]; (2) ballast particles are chosen from the library to meet the particle size distribution following the specification of the “Chinese Code for Design of Heavy haul Railway”; (3) Compaction stage I: one top platen is applied to compact the ballast particles with the compaction strength of 200 kPa, according to the Chinese construction standard [21]; (4) the geometric shape of sleepers are simulated by generating particles at the appropriate location and bonding small particles together as a Clump (super rigid assemblies); (5) Compaction stage II: simulate the train load and exert it on the sleeper particles until the railway ballasted track reaches a stable state. More detailed information about the DEM simulation of the ballast layer can be found in Ref. [22].

Figure 2 shows the initial force chain state of the railway ballasted track, and the lower part is the enlarged view of five sleepers. Each contact force is represented at the contact point by a red line oriented in the direction of the force and with thickness proportional to its force magnitude. The contact forces (red lines) can be observed in the ballast layer under the sleepers, while the contact forces of the crib ballast (ballast between sleepers) are relatively small. The ballast particles in the red lines are the main force chains that withstand the forces transmitted from the sleepers. Usually, the force chains that close to the sleeper are thicker and then the forces dispersed through more contacts of the ballast particles towards the substructure. This force chain structure also means the sleepers contact tightly with ballast particles and the initial state of the ballast layer is well compacted. Furthermore, due to

1 the random distribution and arrangement of ballast particles, the force chains in the ballast layer are variable under
 2 the different sleepers.



3
4
5 **Fig. 2** Initial force chain state of railway ballasted track

6 For this DEM railway ballasted track, the linear contact model and slip model (as described in the PFC manual
 7 [23]) are used to simulate the interactions between the ballast and sleepers. Table 1 lists main parameters of the
 8 DEM railway ballasted track used in this work. The contact stiffness is set to be the same value at 5×10^8 N/m,
 9 including sleeper-ballast, ballast-ballast and wall-ballast contacts. Both the contact stiffness and friction used in this
 10 paper are close to the value in references [24-25]. The sleeper is modelled as a clump, and each disk unit density is
 11 set at 2441 kg/m^3 according to the real sleeper mass. The disk unit density of each ballast is set to 2600 kg/m^3 , and
 12 the bulk density of the ballast bed is around 1800 kg/m^3 , which is consistent with the same void ratio with the
 13 ballast bed in situ.

14 **Table 1** Main parameters of the DEM model

| Parameter name | value | unit |
|--------------------------------|-----------------|-----------------|
| Ballast disk density | 2600 | kg/m^3 |
| Ballast normal/shear stiffness | 5×10^8 | N/m |
| Ballast disk radius | 4 | mm |
| Sleeper particle density | 2441 | kg/m^3 |
| Sleeper normal/shear stiffness | 5×10^8 | N/m |
| Sleeper disk radius | 5 | mm |
| Disk thickness | 1.3 | m |
| Friction | 0.7 | — |
| Viscous Damping | 0.25 | — |

15
16 **2.2 Substructure FDM model**

17 Due to the numerical inability in accurately modelling the track-substructure system with different particles
 18 assemblies and layering using the DEM, the substructure is regarded as an elastic continuum and simulated with the
 19 solid elements in the FLAC [26]. The substructure system consists of 300×100 plane-stress elements, and

1 different parts of the substructure are distinguished by setting different modulus of elasticity. Regarding the
 2 material parameters of the FDM model, a classic isotropic, linear-elastic constitutive model is applied for all the
 3 substructure materials (backfill, structure and subgrade). The substructure material parameters are shown in Table 2.
 4 The dynamic elastic modulus of the subgrade surface layer for transition zone and the wedge-shaped backfill are
 5 chosen as 4000 MPa and 2000 MPa, respectively [4]. Additionally, due to the wave reflections at the boundaries
 6 may affect the dynamic simulation results, the artificial boundary conditions are used in the FDM domain. The
 7 quiet boundary is utilised at the FDM bottom, which is based on the use of independent dashpots in the normal and
 8 shear directions at the model boundaries. Furthermore, the free-field boundary is specified to lateral outer
 9 boundaries of the substructure. The free-field boundary is achieved by generating a one-dimensional grid at the
 10 boundary, and it is equivalent to the effect of an infinite field [26].

11 **Table 2** Main substructure parameters of FDM model [4]

| Parameters | Poisson's ratio | Young's modulus (MPa) | Density (kg/m ³) |
|---|-----------------|-----------------------|------------------------------|
| Surface layer of subgrade for transition zone | 0.3 | 4000 | 2200 |
| Surface layer of subgrade | 0.33 | 500 | 1950 |
| Bottom layer of subgrade | 0.35 | 200 | 1900 |
| Subgrade body | 0.35 | 150 | 1850 |
| Wedge-shaped backfill | 0.3 | 2000 | 2200 |
| Structure | 0.2 | 30000 | 2400 |

12 2.3 Coupling principle

13 As described above, the sleeper and ballast are built with the DEM, and the substructure system is built with the
 14 FDM. And then, a series of interface elements (PFC wall elements) are generated between the DEM and the FDM
 15 (according to the FDM surface node locations) to help implement the coupling process, such that each segment of
 16 wall corresponds to a single segment of the substructure surface at each step. The force-displacement law derives
 17 the contact force acting on the boundary of DEM and FDM. At a given period, the contact force vector F_c , which
 18 represents the interaction between the two parts (as shown in Figure 3), can be resolved into normal (F_c^n) and shear
 19 components vectors (F_c^s) with respect to the contact plane:

$$20 \Delta F_c^s = -k^s \Delta U^s \quad (1)$$

$$21 F_c^n = k^n U^n n_i \quad (2)$$

22 where k^n and k^s are the normal and shear contact stiffness, U^n is the normal contact displacement, ΔF_c^s is
 23 the increment of the shear contact force, ΔU^s is the incremental shear displacement.

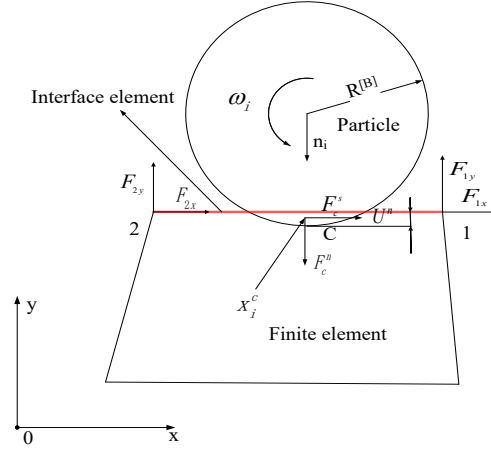


Fig.3 Interaction between DEM particle and FDM element

The new shear contact force is determined by summing the old shear force at the start of each time step with the shear elastic force increment:

$$F_c^s \leftarrow F_c^s + \Delta F_c^s \leq \mu F_c^n \quad (3)$$

where μ is the friction coefficient.

After the normal and shear contact forces between DEM particle and FDM element are obtained according to Eqs. (1) and (2), the force of finite elements nodal is obtained by distributing the interaction contact force through interpolation functions.

The nodal force vector can be defined as

$$\{F\} = [N]^T \{R\} \quad (4)$$

$$\text{with } \{F\} = \{F_{1x} \ F_{1y} \ F_{2x} \ F_{2y}\}, \ [N] = \begin{bmatrix} N_1 & 0 & N_2 & 0 \\ 0 & N_1 & 0 & N_2 \end{bmatrix}, \ \{R\} = \{F_c^s \ F_c^n\}$$

$$\text{where } N_1 = 1 - \frac{x}{l}, \ N_2 = \frac{x}{l}$$

and x is the position of the DEM particle contact with the interface element, l is the length of the interface element, F_{1x} is the force in the x-direction at nodal 1, F_{1y} is the force in the y-direction at nodal 1, F_{2x} is the force in the x-direction at nodal 2, F_{2y} is the force in the y-direction at node 2.

After the contact force at the interface is converted to the nodal force, the translation motion of the element resultant force in continuum and discrete domain can be represented as:

$$F_i^{(t)} = \sum_{j, j \neq i} F_{ij}^{(t)} + F_e = m \ddot{x}_i^{(t)} \quad (5)$$

1 where F_i is the sum of the forces vector at each grid node in FLAC, it includes the external load and the gravity,
 2 and F_i is total unbalanced force vector of each particle in PFC; $\sum_{j,j \neq i} F_{ij}$ is total force that other element force
 3 acting on i element, it can be obtained from the stress-strain constitutive relation in FLAC, and can be calculated
 4 by the contact force-displacement relation in PFC; F_e denotes the external force; m denotes the mass; x_i
 5 denotes the displacement.

6 Then, the explicit central difference scheme is used to solve the equations of motion in discrete and continuum
 7 elements, and the corresponding velocities and displacements can be expressed by

$$8 \quad \dot{x}_i(t + \frac{\Delta t}{2}) = \dot{x}_i(t - \frac{\Delta t}{2}) + \frac{F_i(t)}{m} \Delta t \quad (6)$$

$$9 \quad x_i(t + \Delta t) = x_i(t) + \dot{x}_i(t + \frac{\Delta t}{2}) \Delta t \quad (7)$$

10 The equations of translation motion are presented, and the rotational motion and finite difference form of the
 11 moment almost similar to the translation motion. Accordingly, the contact forces (moments) at the interface
 12 between the two domains are updated and then applied back to the two domains within each time-step. Moreover,
 13 the velocity and displacement are also calculated using the motion equation in two domains according to the update
 14 forces (moments).

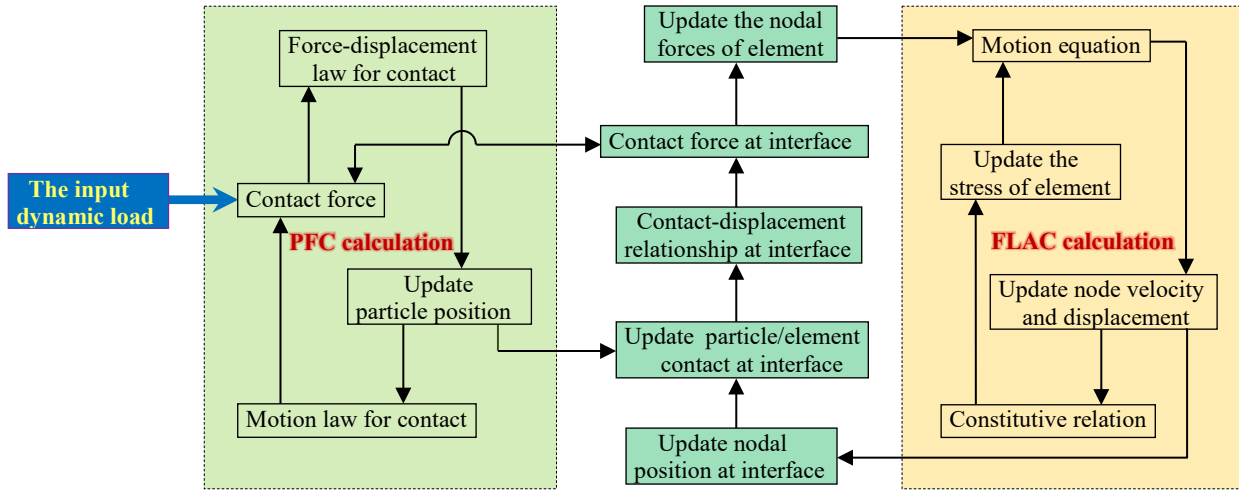


Fig. 4 Flowchart of discrete-continuum coupling calculation

25 The procedure of the coupling simulation is depicted in Figure 4. First, the input dynamic load is applied on
 26 the sleepers, and the positions of the particles are firstly updated based on the force-displacement law in the PFC.
 27 Then the contact forces at the interface are recalculated and distributed to the FLAC interface nodal, and the
 28 velocity and relative displacement in FLAC are evaluated using the motion equation. Afterwards, the boundary

1 nodal velocity and displacement data in FLAC are sent back to PFC to update the interface wall position and
2 contact forces before a new round of calculation begins. In this fashion, the data of the coordinates, velocities, and
3 forces are updated and transmitted between the FLAC and PFC during each cycle, and the coupling simulation is
4 achieved.

5 3. Experimental validation

6 3.1 Field test description and results

7 A field measurement at a transition zone is performed to validate this proposed model when the train is travelling
8 from the tunnel to the normal track. Figure 5 shows the field test site of Suining-Chongqing railway line in China,
9 and records are made when a freight train is passing the test site. The field test is performed at two different specific
10 locations, S1 on the transition section and S2 on the normal track section. The dynamic wheel-rail forces, vertical
11 displacements of sleeper, rail seat loads and the accelerations of the ballast particles and sleepers are measured.
12 Each of the recorded time history contains HXD1 locomotives hauling up to 51 wagons traveling with the speeds at
13 67.2 km/h. The HXD1 locomotive is approximately 35 m long and consists of two identical 4-axle locomotives
14 connected by internal links (each of axles carries a load at 250 kN). The wheel base of the bogie (L_w) is 2.8 m, and
15 the longitudinal distance between the two bogie centers (L_c) is 9 m.



16
17 **Fig. 5** The field test site of the transition zone

18 The measurements using various types of transducers are performed to obtain the responses of track
19 components: (1) dynamic wheel load is measured using strain gauges at the rail and calculated by Wheatstone
20 bridge mounted web (Figure 6a); (2) rail seat load is measured by imbedding a Tekscan sensor under the rail pads
21 (Figure 6b), for more details can be seen in Ref. [27]; (3) sleeper vertical displacements are measured with the
22 contactless NDI Optotrak Certus system which is comprised of a laser transmitter and a position sensitive detector

1 (Figure 6e); (4) sleeper vertical accelerations are measured with piezoelectric accelerometers (Figure 6c); (5)
2 ballast accelerations are measured with an accelerometer embedded in ballast bed, and a designed container is
3 applied to avoid damages to the accelerometer [28]. The ballast acceleration measurement position is placed at 15
4 cm below the sleeper (Figure 6d).

5 The IMC data acquisition system is used to record the signal of wheel-rail forces and accelerations with the
6 frequency rate of 5000 Hz and 1000 Hz, respectively. A computer installed with the acquisition software is adopted
7 to acquire the measured data. The Tekscan sensor can sustain the maximum pressure up to 200 MPa and provided
8 the sampling frequency up to 100 Hz. The NDI Optotrak measurement is able to acquire the minimum
9 displacement of 0.1 mm, and the acquisition frequency rate of 100 Hz is used. Particularly, the diverse measuring
10 systems are pre-calibrated in the laboratory afterwards utilised in the field test.



11 **Fig. 6** Detail of track instrumentation at transition zone: (a) dynamic load on rail; (b) rail seat loads; (c) sleeper acceleration; (d)
12 special box for accelerometer in ballast bed; (e) sleeper displacement
13

14 Figure 7 presents the measured data under the train dynamic wheel loads at the transition section (S1), and the
15 peak value of the dynamic loads on rail caused by the front locomotive is about 153.64 kN. Also, the maximum
16 amplitude of 166.45 kN is measured at the embankment section (S2), which is in agreement with the conclusion of
17 existing studies, which is the influence of track stiffness on the dynamic wheel load is not obvious [1,2]. Therefore,
18 the same rail seat load measured at the S1 section can be applied into the numerical model of all sleepers as
19 external loads. As shown in Figure 8, the maximum amplitude of the rail seat load induced by the front locomotive
20 is 71.1 kN, which is nearly 46.3% of the dynamic wheel load. According to the earlier studies [27, 29], the largest
21 rail seat load is around 40-50% of the wheel load which means that the wheel-rail force transferred to the rail pad is
22 reasonable.

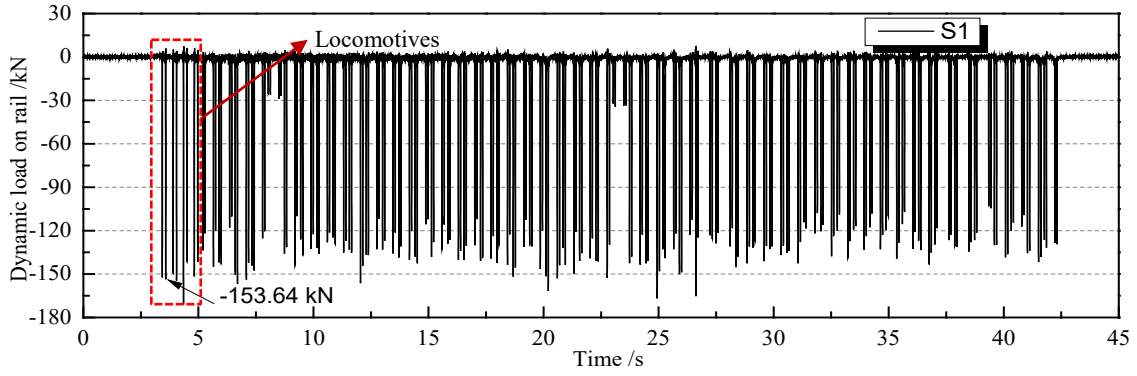


Fig. 7 Measured dynamic load on the rail

From Figure 7 and 8, it can be seen that the dynamic loads on rail and the rail seat loads repeat similarly for every pair of enclosed bogies. In other words, the loads of every two enclosed bogies of one vehicle are approximate, because of the similar coach car configuration and axle load. The variability of each load cycle possibly results from diverse factors. On one hand, the static loads of each axle are slightly different depending on the vehicle counterweight. On the other hand, the random system dynamic responses for high frequencies produce extra forces on the train-track interaction because of the wheel/rail irregularities. The study conducted in Ref. [30] found that the effect of the full train (comprising 12 bogies) was almost identical to the superimposition of the effect of 12 times a single bogie. Therefore, one locomotive passing the track is simulated in this work, instead of modeling the entire train, to reduce the calculation time.

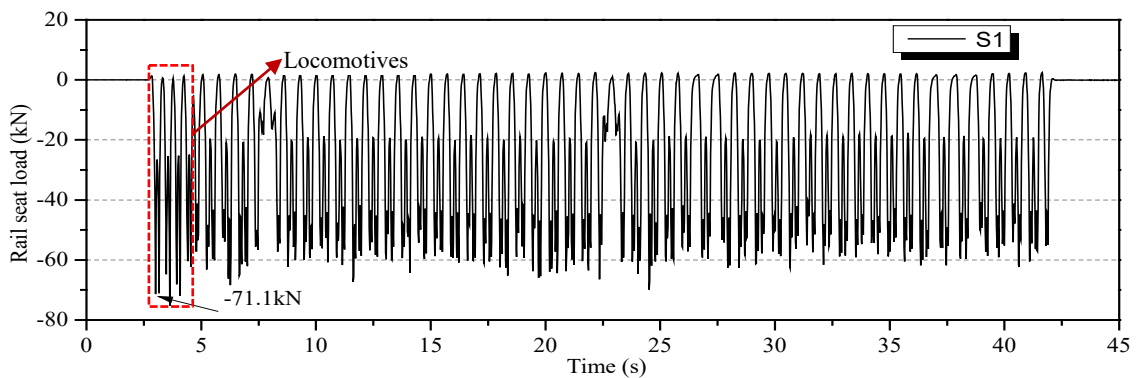
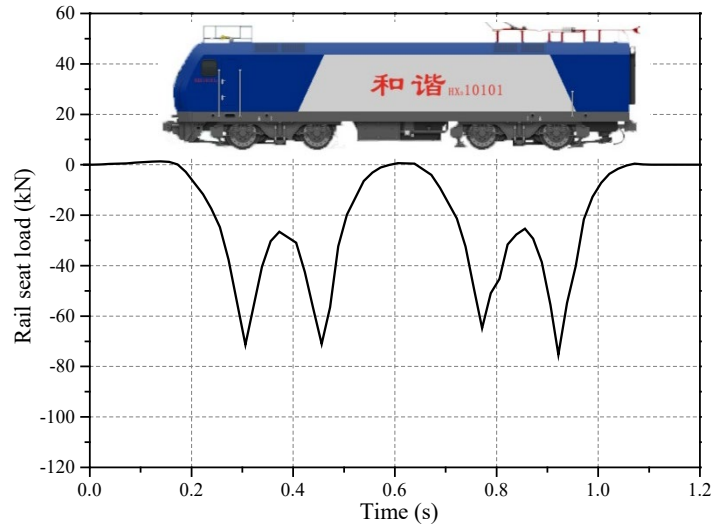


Fig. 8 Measured rail seat load

3.2 Sequential loading to coupled model

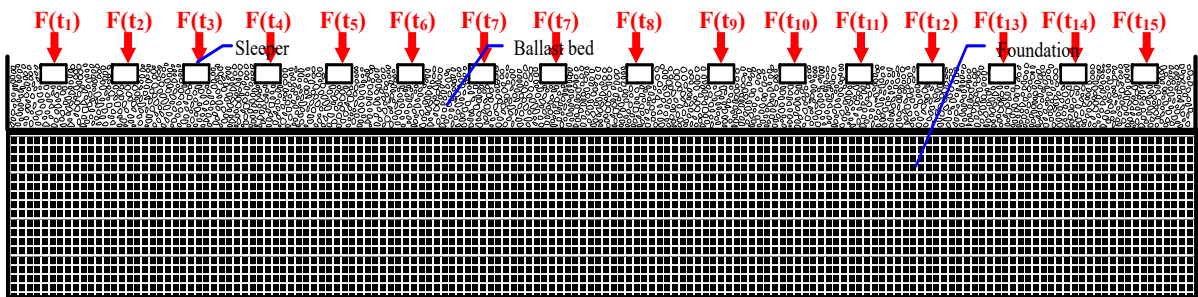
Due to the discontinuous support of the rail, the traffic loads induced by the movement of the train on rail is first transferred to the sleeper via fasteners, then to the substructure. During the passage of the train, the moving loads on the rail are converted into a vertical time-varying rail seat loads applied to each sleeper. Figure 9 shows the rail seat load induced by the front HXD1 locomotive, and the peak values when four wheelsets pass by can be clearly

1 distinguished. As described above, the variation of the substructure stiffness at railway transition zones barely
 2 influence the dynamic wheel load at the rail. Thus, the same time-varying rail seat load is applied into each sleeper
 3 with a time shift to simulate the train passage. The effectiveness of the applied sequential loadings at sleeper
 4 positions has been verified by Bian et al. [31] with field measurements.



5
6 **Fig. 9** Rail seat load induced by one locomotive

7 As shown in Figure 10, the rail seat load $F(t)$ is exerted on to all the sleepers with a specific time shift.
 8 Assuming the locomotive is running at a constant speed from left to right, thus, the first sleeper on the left
 9 experiences the force, afterwards the second and third sleepers will undergo the loads after time intervals of 0.032 s
 10 and 0.064 s, respectively. The rest sleepers can be deduced by analogy. In this way, one locomotive passing through
 11 the transition zone is simulated, and the dynamic response of track components induced by moving train can be
 12 obtained.

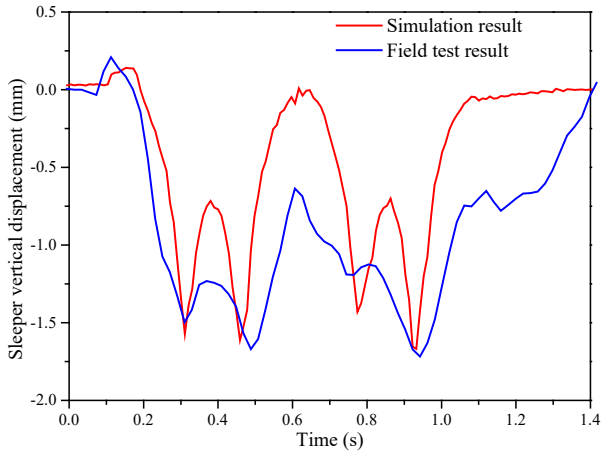


13
14 **Fig 10.** Schematic of applying the rail seat loads in numerical model

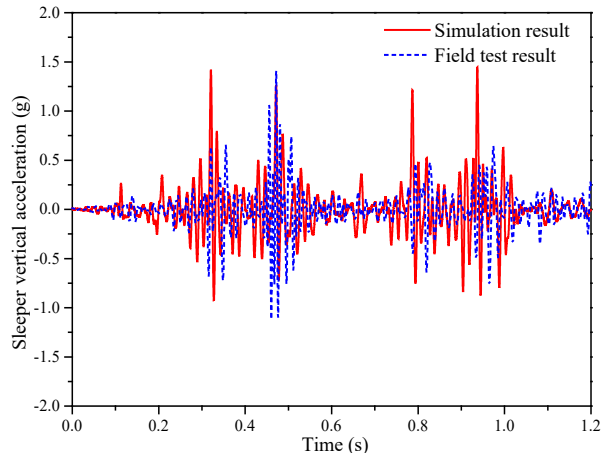
15 3.3 Model validation

16 For the model validation, the numerical results are compared with those from the field measurements. Because the
 17 random nature of the dynamic response for high frequencies due to track and wheel irregularities (which are out of

1 this study scope), and the sampling frequency rate of 100 Hz is applied to the rail seat load (external excitation of
 2 this numerical model), the low-pass filters with the frequencies of 100 Hz are applied to the recorded acceleration
 3 of the sleeper and ballast in time histories.



4
5 **Fig. 11** Sleeper displacement at position S1



6
7 **Fig. 12** Sleeper accelerations at position S1

8 Figure 11 shows the comparison between the numerical results and measured ones for the vertical sleeper
 9 displacements at the location S1. The peak values of the numerical results are close to the field test, near 1.7 mm.
 10 The distribution of the time-varying amplitude shows good agreement with that from the field measurement, while
 11 there is a certain difference at the top of the waveform. This may be due to the field test results of sleeper time
 12 history curve cannot quickly return to the original position maybe caused by the poor elastic support of the ballast
 13 bed. Furthermore, the vibration of the laser transmitter caused by the train passing also has some effect on the
 14 measurement results. As shown in Figure 12 and Figure 13, the numerical results of sleeper acceleration at location
 15 S1 and S2 also show a good agreement with the field measurements, and the difference between the field and
 16 simulation results is about 2.9 % and 31%, respectively. In addition, the field measurement results also show that
 17 the acceleration of the sleeper on the embankment is slightly larger than that on the wedge-shape backfill. Figure 14
 18 presents the results of ballast accelerations at position S2. The peak acceleration results from the numerical
 19 simulation are somewhat overestimated when compared with the field test results, and the measurement results of
 20 the ballast acceleration at S1 also show a similar phenomenon. This is mainly due to the coupled model is
 two-dimensional, which only allows the ballast to move in a plane and contacts force between ballast particles
 cannot be shared by other particles in the direction of perpendicular to the plane.

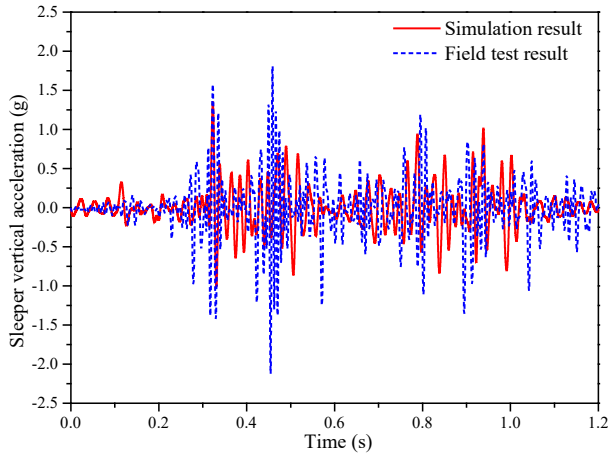


Fig. 13 Sleeper accelerations at position S2

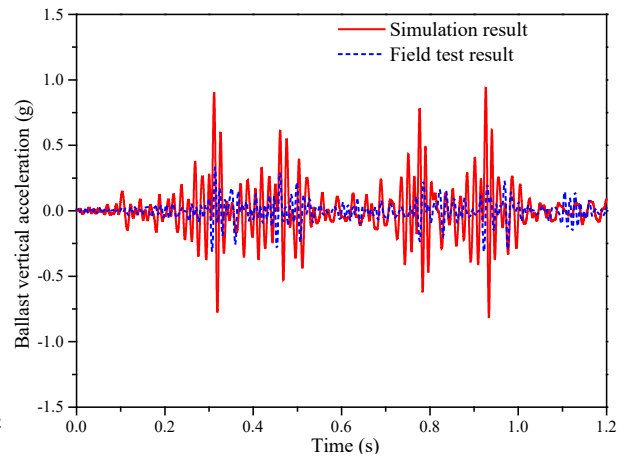


Fig. 14 Ballast accelerations at position S2

Figure 15-16 present the comparison of frequency spectra of sleeper and ballast acceleration between the field test results and simulation results. It can be seen that the frequencies of 2.0 Hz and 6.5 Hz are obvious for sleeper and ballast acceleration spectrum, which are induced by bogies and axles, respectively. Since L_c is 9 m and L_w is 2.8 m, the loading frequencies of the moving vehicle (v/L_c and v/L_w , $v = 67.2$ km/h) are 2.1 Hz and 6.7 Hz, respectively. The difference of the acceleration spectra in the frequency domain is mainly caused by the different support and contact states of the sleeper and the ballast. In summary, the numerical simulation results show a relatively good agreement with the field test results, and this coupled model is validated.

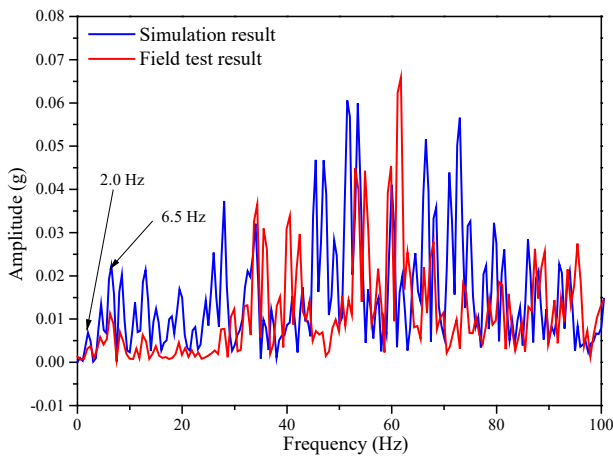


Fig. 15 Sleeper acceleration spectrum at position S1

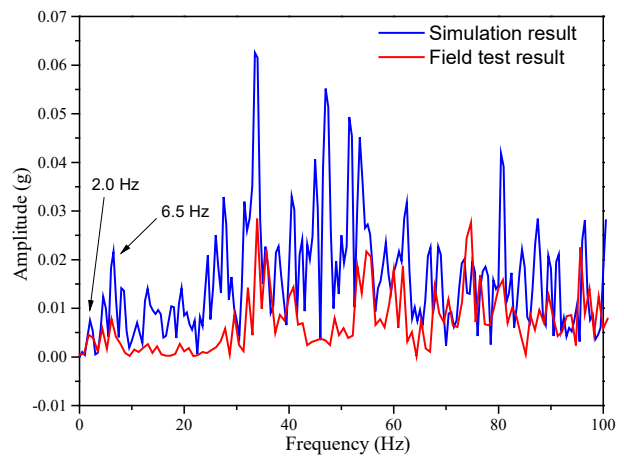
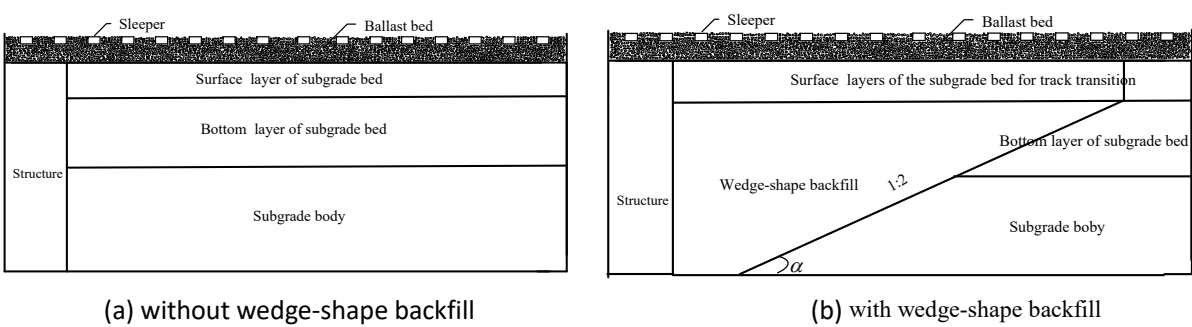


Fig. 16 Ballast acceleration spectrum at position S2

4. Influence of wedge-shape backfill on track dynamic behaviour

Based on this validated model, the dynamic behaviours of track components with respect to two cases are analysed: one has the wedge-shape backfill, the other does not have the wedge-shape backfill. Figure 17 shows the schematic of two track transition models. In the cases of wedge-shape backfill absence, the structure section directly connects to three layers of subgrade. Consequently, the effects of wedge-shape backfill on sleeper displacement, sleeper

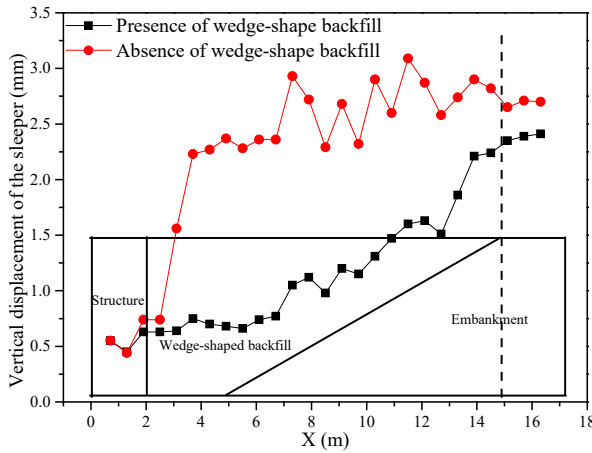
1 vertical acceleration, ballast displacement, ballast vertical acceleration, substructure surface stress and substructure
 2 surface displacement will be explored.



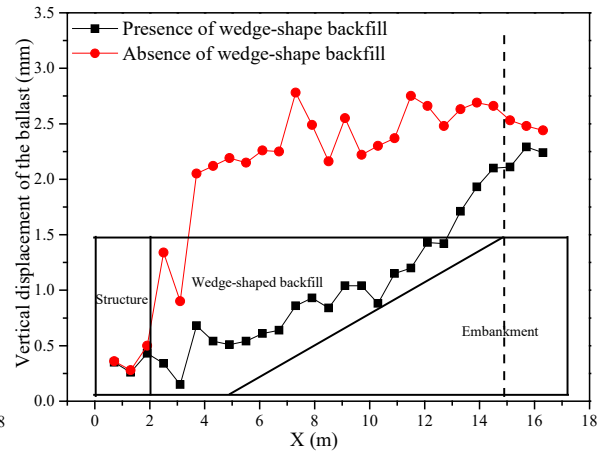
3
 4 (a) without wedge-shape backfill (b) with wedge-shape backfill
 5 **Fig. 17** Schematic of the two track transition models

6 *4.1 Dynamic characteristics along the transition zones*

7 Figures 18 and 19 show the maximum displacements of the sleeper and ballast along the track in the presence or
 8 absence of the wedge-shape backfill, and the monitoring ballast particles are respectively located below each
 9 sleeper and 0.15 m below the sleeper. As shown in Figures 18 and 19, on the absence of wedge-shaped backfill, the
 10 displacements of the sleepers and ballast particles increase significantly about 2 m away from the structure section
 11 to reach its maximum value. The variation from $x = 6$ m to $x = 14$ m is mainly caused by the supporting condition
 12 of ballast bed and is consistent with the measurements [32-33]. At the cross-section of the structure and the
 13 embankment, the vertical displacements of sleepers increase abruptly from 0.75 mm to 2.25 mm, and the
 14 displacement of the ballast increases sharply from 0.5 mm to 2.1 mm. The displacement of track components varies
 15 abruptly in a short length, which directly affects the train running safety and causes destructive effects to the tracks.
 16 When it comes to the presence of wedge-shaped backfill, the track stiffness gradually decreases from the
 17 higher-stiffness structure section to lower-stiffness embankment section. Therefore, the displacements of the
 18 sleeper and the ballast gradually increase from a low value at the structure section to high value at the embankment
 19 section, which is beneficial to the steady running of the train and reduce the impacts on the track.

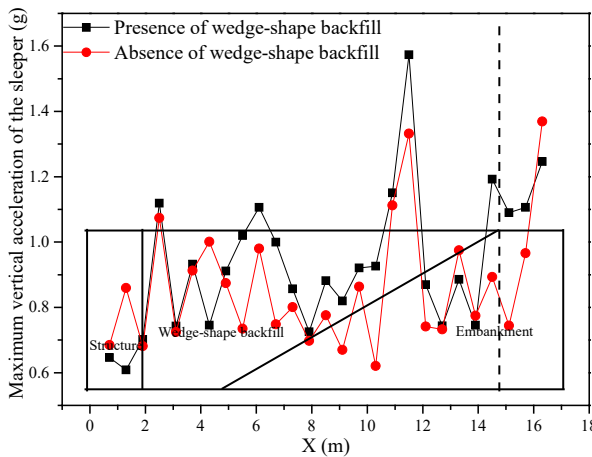


1
2 **Fig. 18** Longitudinal distribution of sleeper displacement

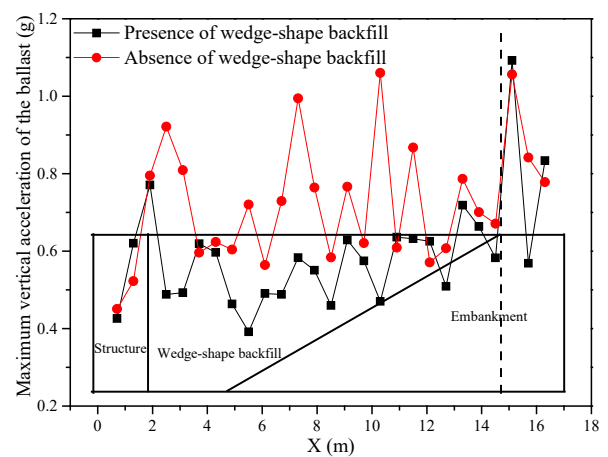


3 **Fig. 19** Longitudinal distribution of ballast displacement

4 The maximum accelerations of the sleeper and the ballast in the two cases (presence and absence of
 5 wedge-shape backfill) are presented in the Figures 20 and 21, and the maximum value is collected from the
 6 time-domain responses after 100 Hz low filtration. In Figure 20, the vertical acceleration of the sleeper varies from
 7 0.62 g to 1.34 g in the case of wedge-shape backfill absence, while the vertical acceleration of the sleeper varies
 8 from 0.61 g to 1.57 g in the case of wedge-shape backfill presence. As can be seen from Figure 21, the presence of
 9 wedge-shape backfill apparently decreases the fluctuation of ballast acceleration, attributing to the gradual
 10 changing of the substructure stiffness that provides more stable particle interlocking [17]. Additionally, it can be
 11 seen from Figure 21 that the gradual increase of the ballast accelerations from structure section to embankment
 section emerges against the presence of the wedge-shape backfill.



12 **Fig. 20** Longitudinal distribution of sleeper acceleration

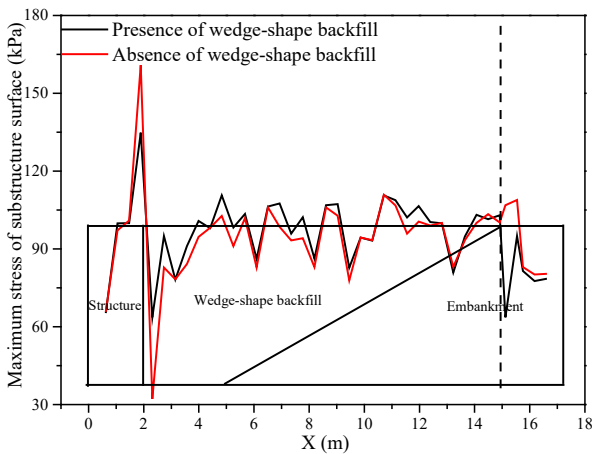


13 **Fig. 21** Longitudinal distribution of ballast acceleration

14 4.2 The substructure dynamic characteristics along the transition zones

15 The vertical stress and displacement (maximum value) at the substructure surface are shown in Figure 22 and 23,
 16 respectively. Figure 23 presents the vertical stress distribution at the substructure surface with and without the
 17 wedge-shape backfill, in which the stress amplitude coincides well with those in situ [34-35]. The results show that

1 the largest vibration of the vertical stress at the substructure surface appears at $x = 2$ m, which is the connection of
 2 two different structures. It also indicates that this is a weak area of the transition zone. In the absence of the
 3 wedge-shaped backfill, the vertical stress at the substructure surface reaches 165 kPa at the structure section firstly,
 4 and then decrease to 27 kPa. However, in the case where the wedge-shaped backfill is considered, the difference of
 5 substructure surface maximum stress near the structure and embankment joining point decreases by 54%. The
 6 maximum displacement distribution on the substructure surface along the track is illustrated in Figure 23. As shown
 7 in Figure 23, the maximum displacement of the substructure surface is 0.02 mm at the structure section in two cases
 8 (with or without the wedge-shaped backfill), then the value increases to 1.8 mm within a short length of 4 m when
 9 the wedge-shaped backfill is absent. In the presence of the wedge-shaped backfill, the vertical displacement value
 10 at the substructure surface is gradually increased to 1.64 mm from the structure section to embankment section,
 11 which is also the reason for the smooth transition of sleepers and ballast particles.



12
13 **Fig. 22** Distribution of subgrade surface stress

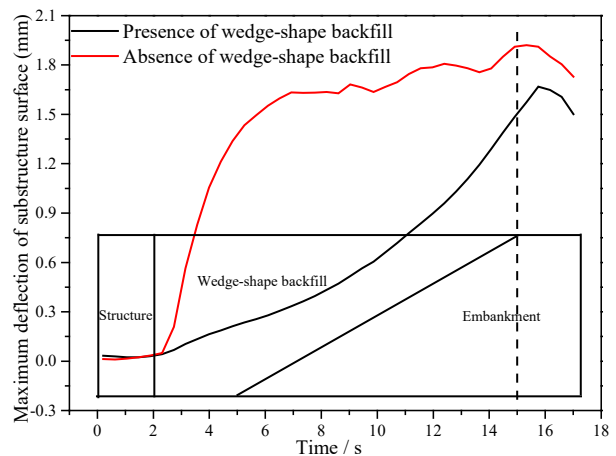
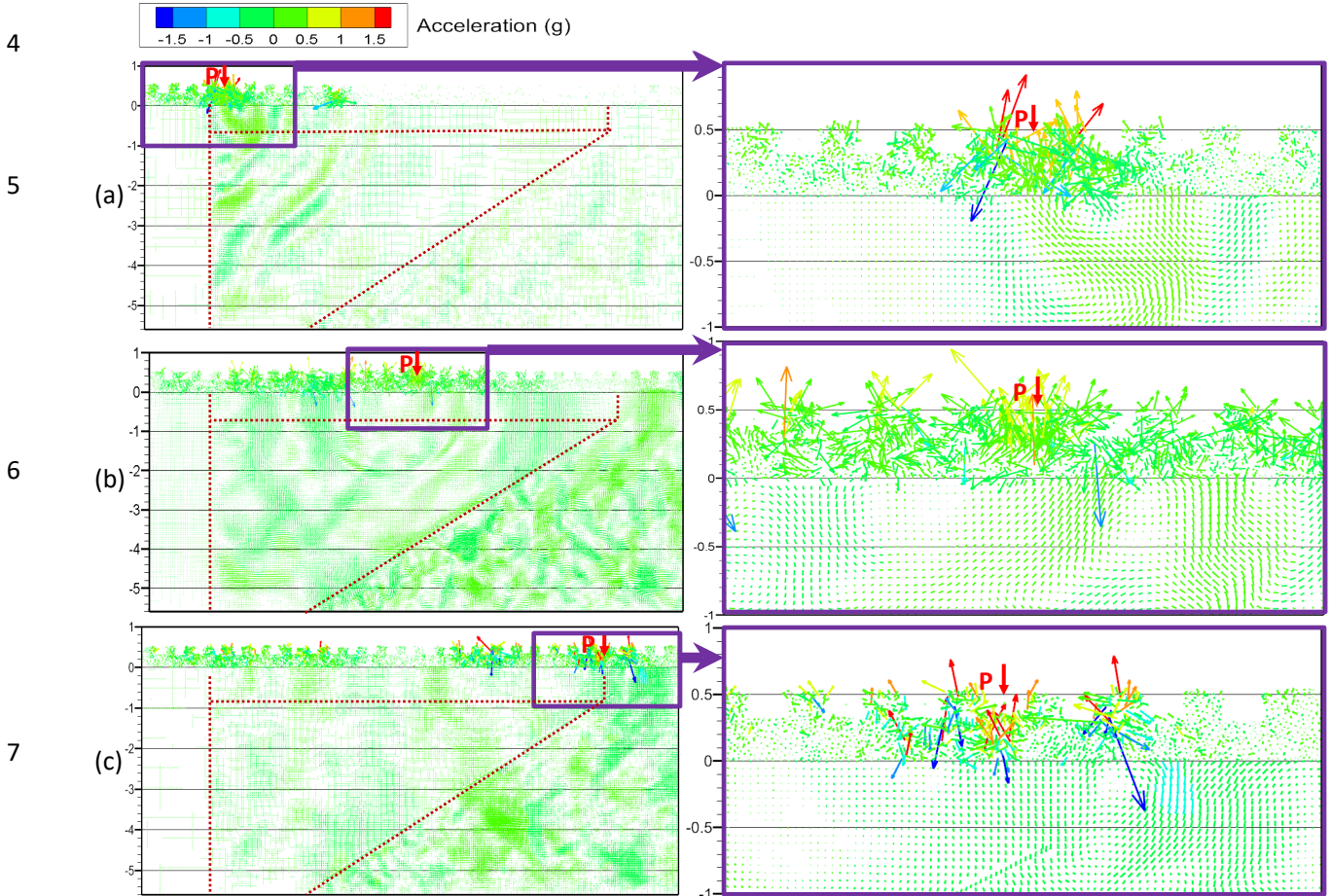


Fig. 23 Distribution of subgrade surface displacement

14 4.3 Spatial distribution of the acceleration and velocity vector

15 Figure 24 shows the ballast particle acceleration vector of the transition zone model under the condition of vehicle
 16 travelling from the higher stiffness to the lower, and the symbol P expresses the dynamic load of the first axle.
 17 The local details of 7 sleepers around a central sleeper are also shown when the first wheelset is arriving on. As
 18 shown in Figure 24, when the wheelset arrives upon a sleeper, the accelerations of the ballast particles near this
 19 sleeper are generally bigger than those at other regions. However, due to the interlocking between ballast particles,
 20 a few small ballast particles are suspended by the surrounding ballast. Thus, the acceleration of these ballast
 21 particles may be even larger than the areas where the wheelset loads are directly applied. Figure 24 indicates that
 22 the vector distribution of the ballast acceleration is rather inhomogeneous, because of the complicated contacts
 23 between ballast particles, and the region distribution of substructure acceleration is also irregular. Furthermore, the

1 phenomenon of the wave transfer in the substructure can be seen in Figure 24 (a) and (b). In Figure 24 (a), the
 2 direction of wave propagation is toward to the embankment, due to the blocking of rigid structure. It may cause the
 3 substructure soil moving away from the abutment under the long-term train load.

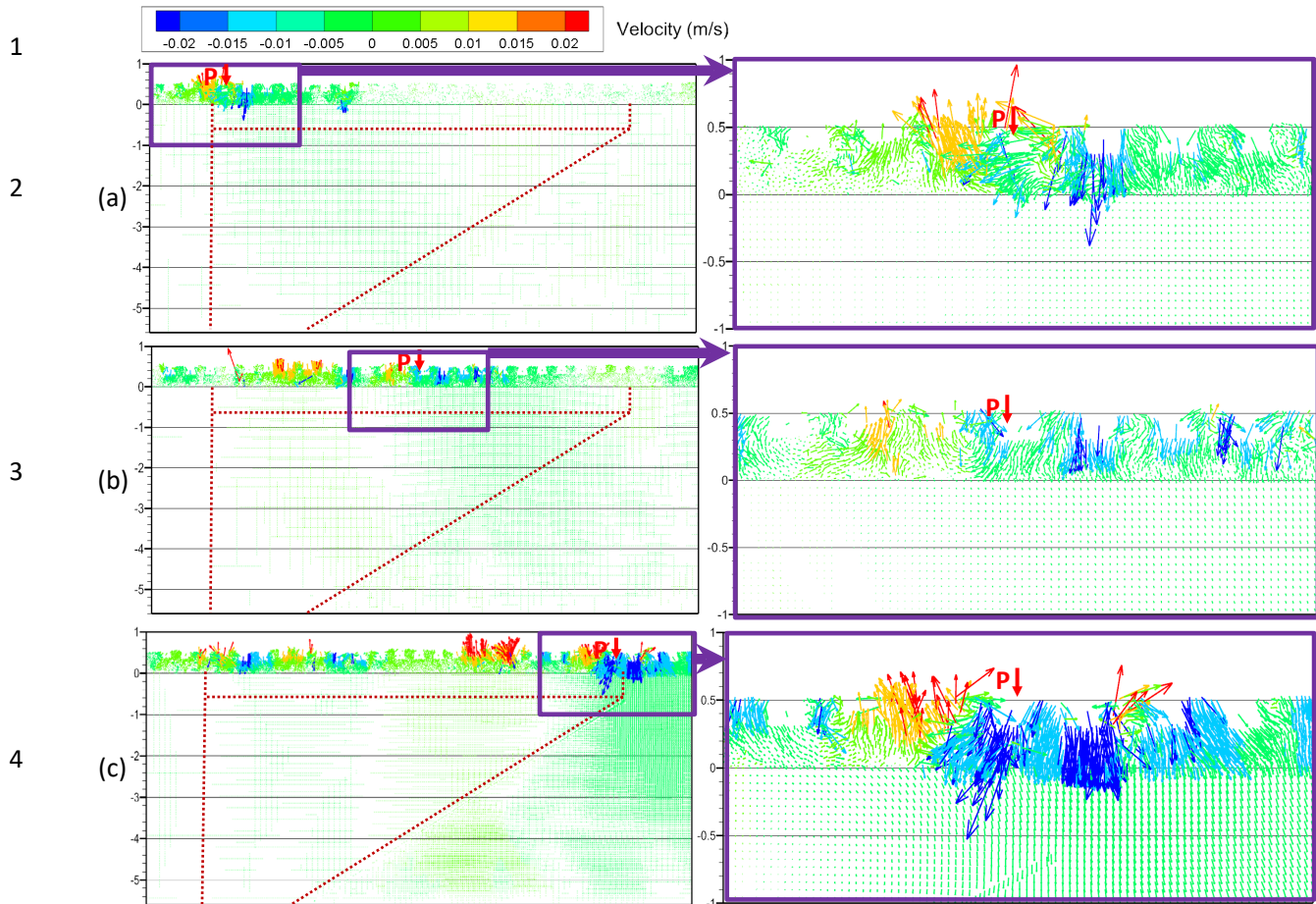


8 **Fig. 24** The acceleration vector graph under first wheelset arrives at different positions: (a) the beginning of wedge-shape backfill; (b)
 9 the middle of wedge-shape backfill; (c) the end of wedge-shape backfill.

10 Figure 25 shows the velocity vector of the transition zone when train loads travel from the structure section
 11 with higher stiffness to the embankment section with lower stiffness. When the wheelset arrives at a sleeper, it will
 12 induce the ballast and substructure moving downward at the areas of this sleeper and three sleepers ahead. The
 13 downward ballast particles movement will affect the nearby ballast particles, which may cause the ballast particles
 14 between the sleepers suffering the risk of splashing, and the phenomenon of ballast flight is more likely to occur for
 15 the ballast particle behind the wheelset. Besides, in comparison of the velocity vector of the transition zone at the
 16 different positions, it can be observed that the velocity responses of the ballast and the substructure gradually
 17 increase when the wheelset moves from the rigid structure to the soft embankment.

18

19



5 **Fig. 25** The velocity vector graph under first wheelset arrives at different positions: (a) the beginning of wedge-shape backfill; (b) the
6 middle of wedge-shape backfill; (c) the end of wedge-shape backfill.

7 **5. Conclusions**

8 In this paper, a coupled DEM-FDM model is presented to better understand the macro-meso mechanical behaviour
9 of railway transition zones, moreover, a field measurement is performed in Sui-Yu railway line to validate this
10 proposed model. The field measurements reveal that the dynamic rail seat load is nearly 46.3% of the dynamic
11 wheel load and the influence of track stiffness on the dynamic wheel load at the rail is not obvious. The measured
12 results of rail seat loads are used as external loads to the coupled DEM-FDM model. After comparing the
13 simulation results of the dynamic response of track components to the field test result, it is confirmed that the
14 hybrid simulation method combining DEM and FDM is feasible to analyse the dynamic behaviour of railway track
15 transitions.

16 Moreover, the numerical simulation results indicate that the existence of wedge-shape backfill is useful to
17 diminish the negative effects of the abrupt dynamic displacement change between the structure and the
18 embankment, and can reduce the variations of the track components acceleration and substructure surface stress.
19 Specifically, the difference of substructure surface maximum stresses near the structure and embankment joining

1 point decreases by 54%. It can be seen from mesoscopic behaviour that the wheelset only affects the ballast
2 particles near the sleeper and the acceleration distribution of ballast particles is non-uniform in ballast bed and
3 substructure. Moreover, the fluctuation of acceleration vector in the substructure causes the soil near the rigid
4 structure to move towards the embankment. Additionally, by comparing to the velocity vectors of the transition
5 zone when the wheelset arrives at different locations, it can be observed that the velocity of the ballast particles
6 gradually increases when the wheelset is traveling from the structure to the embankment. Thus, the design of the
7 wedge-shaped backfill can improve the track components dynamic performance, and more attentions should be
8 paid to the connection area between different structures in transition zone.

9 In conclusion, it can be seen that the combined DEM/FDM structure-embankment transition zones model can
10 be used to analyse the macro-meso mechanical behaviour of track components and reveal the dynamic difference of
11 the transition zone with and without wedge-shape backfill. Furthermore, this research shows the potential to
12 explore the effect of the different substructure forms on the quality of transitions, to reveal the physical
13 deterioration mechanisms and to provide new perspectives on the differential settlement of transition zone, which
14 will be substantively performed as a further step.

15 **Acknowledgement**

16 This research is supported by National Natural Science Foundation of China [Grant No. 51578469 and U1234209];
17 Chinese Program of Introducing Talents of Discipline to Universities (111 Project, Grant No.B16041) and Research
18 Program of State Key Laboratory of Traction Power [Grant No. 2015TPL-T12 and TPL2009].

19 **Declarations of interest**

20 None.

21 **References**

- 22 [1] X. Lei and L. Mao. Dynamic response analyses of vehicle and track coupled system on track transition of
23 conventional high speed railway. *Journal of Sound & Vibration*, 2004, 271(s3-5): 1133-1146.
- 24 [2] J.A. Zakeri and V. Ghorbani. Investigation on dynamic behavior of railway track in transition zone. *Journal of*
25 *Mechanical Science & Technology*, 2011, 25(2): 287-292.
- 26 [3] L. Xu, L. Xin, Z. Yu and Z. Zhu. Construction of a dynamic model for the interaction between the versatile
27 tracks and a vehicle. *Engineering Structures*, 2020, 206, 110067.
- 28 [4] Y. Shan, Y. Shu, S.H. Zhou. Finite-infinite element coupled analysis on the influence of material parameters on
29 the dynamic properties of transition zones. *Construction and Building Materials*, 2017, 148: 548-558.
- 30 [5] H. Wang and V. Markine. Modelling of the long-term behaviour of transition zones: Prediction of track
31 settlement. *Engineering structures*, 2018, 156, 294-304.

- 1 [6] R. Sañudo, M. Cerrada, B. Alonso and L. dell'Olio. Analysis of the influence of support positions in transition
2 zones. *A numerical analysis. Construction and Building Materials*, 2017, 145: 207-217.
- 3 [7] M. Shahraki, C. Warnakulasooriya and K.J. Witt. Numerical study of transition zone between ballasted and
4 ballastless railway track. *Transportation Geotechnics*, 2015, 3: 58-67.
- 5 [8] L. Xu, Z. Yu and C. Shi. A matrix coupled model for vehicle-slab track-subgrade interactions at 3-D space. *Soil
6 Dynamics and Earthquake Engineering*, 2020, 128: 105894.
- 7 [9] C.A. Ribeiro, R. Calçada and R. Delgado. Experimental assessment of the dynamic behaviour of the train-track
8 system at a culvert transition zone. *Engineering Structures*, 2017, 138: 215-228.
- 9 [10] B.Z. Coelho, P. Hölscher, J. Priest, W. Powrie and F. Barends. An assessment of transition zone performance.
10 *Proceedings of the Institution of Mechanical Engineers Part F Journal of Rail & Rapid Transit*, 2011, 225(1):
11 129-139.
- 12 [11] J.N. Varandas, P. Hölscher and M.A.G. Silva. Dynamic behaviour of railway tracks on transitions zones.
13 *Computers & Structures*, 2011, 89(13-14): 1468-1479.
- 14 [12] D. Mishra, Y. Qian, H. Huang and E. Tutumluer. An integrated approach to dynamic analysis of railroad track
15 transitions behavior. *Transportation Geotechnics*, 2014, 1(4): 188-200.
- 16 [13] J. Shi, M.P.N. Burrow, A.H. Chan and Y.J. Wang. Measurements and simulation of the dynamic responses of a
17 bridge-embankment transition zone below a heavy haul railway line. *Proceedings of Institution of Mechanical
18 Engineers Part F Journal of Rail & Rapid Transit*, 2013, 227(3): 254-268.
- 19 [14] P. Hu, C. Zhang, S.J. Chen, Y. Wang, W. Wang, and W.H. Duan. Dynamic responses of bridge-embankment
20 transitions in high speed railway: Field tests and data analyses. *Engineering Structures*, 2018, 175, 565-576.
- 21 [15] Y. Guo, C. Zhao, V. Markine, G. Jing, and W. Zhai. Calibration for discrete element modelling of railway
22 ballast: A review. *Transportation Geotechnics*, 2020, 100341.
- 23 [16] Y. Qian, E. Tutumluer, Y.M. Hashash, J. Ghaboussi and D.D. Davis. Ballast settlement ramp to mitigate
24 differential settlement in a bridge transition zone. *Transportation Research Record: Journal of the
25 Transportation Research Board*, 2015, 2476: 45-52.
- 26 [17] C. Chen and G. McDowell. An investigation of the dynamic behaviour of track transition zones using discrete
27 element modelling. *Proceedings of the Institution of Mechanical Engineers Part F Journal of Rail & Rapid
28 Transit*. 2016, 230(1): 117-128.
- 29 [18] National Railway Administration of P.R. Design code for heavy haul railway. TB 10625-2017, China Railway
30 Publishing, Beijing, 2017 (in Chinese).
- 31 [19] Y. Guo, V. Markine, X. Zhang, W. Qiang, and G. Jing. Image analysis for morphology, rheology and
32 degradation study of railway ballast: A review. *Transportation Geotechnics*, 2019, 18: 173-211.
- 33 [20] C. Shi, C. Zhao, X. Zhang and A. Andersson. Analysis on dynamic performance of different track transition
34 forms using the discrete element/finite difference hybrid method. *Computers & Structures*, 2020, 230, 106187.
- 35 [21] National Railway Administration of P.R. Standard for constructional quality acceptance of railway track
36 engineering. TB 10413-2003, China Railway Publishing, Beijing, 2003 (in Chinese).
- 37 [22] C. Shi, C. Zhao, X. Zhang and Y. Guo. Coupled discrete-continuum approach for railway ballast track and
38 subgrade macro-meso analysis. *International Journal of Pavement Engineering*, 2020, 1-16.
- 39 [23] Itasca Consulting Group, Inc. Particle Flow Code in 2 Dimensions, version 3.1, User's Manual, 2004.
- 40 [24] X. Zhang, C.F. Zhao and W.M. Zhai. Dynamic behavior analysis of high-speed railway ballast under moving
41 vehicle loads using discrete element method. *International Journal of Geomechanics*, 2017, 17(7):1-14.
- 42 [25] B. Indraratna, P. Thakur, J. Vinod. Experimental and numerical study of railway ballast behavior under cyclic
43 loading. *International Journal of Geomechanics*, 2010, 10(4): 136-144.
- 44 [26] Itasca Consulting Group, Inc. Fast Language Analysis of Continua in 2 Dimensions, Version 5.0, User's

- 1 Manual, 2005.
- 2 [27] X. Zhang, C. Zhao, X. Ren, Y. Feng, C. Shi and W.M. Zhai. Experimental investigation on the characteristics
3 of the dynamic rail pad force and its stress distribution in the time and frequency domain. Proceedings of the
4 Institution of Mechanical Engineers, Part F: Journal of Rail and Rapid Transit, 2019, 0(0): 1-13.
- 5 [28] Zhai, W.M., Wang, K.Y., and Lin, J.H. (2004). Modelling and experiment of railway ballast vibrations. Journal
6 of Sound Vibration, 270(4-5), 673-683.
- 7 [29] A. Paixão, E. Fortunato and R. Calçada. Transition zones to railway bridges: track measurements and
8 numerical modelling. Engineering structures, 2014, 80: 435-443.
- 9 [30] A. Paixão, E. Fortunato, R. Calçada. A numerical study on the influence of backfill settlements in the train
10 track interaction at transition zones to railway bridge. Proceedings of the Institution of Mechanical Engineers
11 Part F Journal of Rail & Rapid Transit, 2016, 230(3): 866-878.
- 12 [31] X. Bian, H. Jiang, C. Cheng, Y. Chen, R. Chen and J. Jiang,. Full-scale model testing on a ballastless
13 high-speed railway under simulated train moving loads. Soil Dynamics and Earthquake Engineering, 2014, 66,
14 368-384.
- 15 [32] B. Coelho, J. Priest, P. Holscher and W. Powrie. Monitoring of transition zones in railways. Proceedings of the
16 Institution of Mechanical Engineers, Part F: Journal of Rail and Rapid Transit, 2009. 13-22.
- 17 [33] D. Bowness, A.C. Lock, W. Powrie, J.A. Priest, D.J. Richards. Monitoring the dynamic displacements of
18 railway track. Proceedings of the Institution of Mechanical Engineers, Part F: Journal of Rail and Rapid
19 Transit, 2017, 221(1), 13-22.
- 20 [34] F. Xu, Q. Yang, W. Liu, W. Leng, R. Nie, H. Mei. Dynamic Stress of Subgrade Bed Layers Subjected to Train
21 Vehicles with Large Axle Loads. Shock and Vibration, 2018.
- 22 [35] R.P. Chen, J.M. Chen, H.L. Wang. Recent Research on the Track-Subgrade of High-Speed Railways. Journal
23 of Zhejiang University Science A, 2014, 15(12), 1034-1038.
- 24